

## Article

# Computation and Analysis of an Offshore Wind Power Forecast: Towards a Better Assessment of Offshore Wind Power Plant Aerodynamics

Yongnian Zhao <sup>1</sup>, Yu Xue <sup>1,\*</sup>, Shanhong Gao <sup>2</sup> , Jundong Wang <sup>1</sup>, Qingcai Cao <sup>3</sup>, Tao Sun <sup>3</sup> and Yan Liu <sup>3</sup>

<sup>1</sup> College of Engineering, Ocean University of China, Qingdao 266100, China; zhaoyongnian4920@stu.ouc.edu.cn (Y.Z.); sakura\_ouc@stu.ouc.edu.cn (J.W.)

<sup>2</sup> College of Oceanic and Atmospheric Sciences, Ocean University of China, Qingdao 266100, China; gaosh@ouc.edu.cn

<sup>3</sup> CDT Renewable Energy Science and Technology Research Institute, Beijing 100040, China; dt\_cqc@126.com (Q.C.); suntao@cdt-eri.com (T.S.); liuyan@cdt-eri.com (Y.L.)

\* Correspondence: xueyu7231@ouc.edu.cn

**Abstract:** For the first time, the Weather Research and Forecast (WRF) model with the Wind Farm Parameterization (WFP) modeling method is utilized for a short-range wind power forecast simulation of 48 h of an offshore wind farm with 100 turbines located on the east coast of the China Yellow Sea. The effects of the horizontal multi-grid downsize method were deployed and investigated on this simulation computation. The simulation was validated with the field data from the Supervisory Control and Data Acquisition (SCADA) system, and the results showed that the horizontal mesh downsize method improved the accuracy of wind speed and then wind power forecast. Meanwhile, the wind power plant aerodynamics with turbine wake and sea–land shore effects were investigated, where the wake effects from the wind farm prolonged several miles downstream, evaluated at two wind speeds of 7 m/s and 10 m/s instances captured from the 48 h of simulation. At the same time, it was interesting to find some sea–land atmospheric effects with wind speed oscillation, especially at the higher wind speed condition. Finally, the research results show that the WRF + WFP model for the wind power forecast for production operation may not be ready at this stage; however, they show that the methodology helps to evaluate the wind power plant aerodynamics with wake effects and micrometeorology of the sea–land interconnection region. This plant aerodynamics study set the stage for a wake turbine interaction study in the future, such as one utilizing the NREL FAST.FARM tool.

**Keywords:** mesh downsize for micrometeorology wind speed simulation; wind power forecast; offshore wind power plant aerodynamics



**Citation:** Zhao, Y.; Xue, Y.; Gao, S.; Wang, J.; Cao, Q.; Sun, T.; Liu, Y. Computation and Analysis of an Offshore Wind Power Forecast: Towards a Better Assessment of Offshore Wind Power Plant Aerodynamics. *Energies* **2022**, *15*, 4223. <https://doi.org/10.3390/en15124223>

Academic Editors: Sergio Ulgiati, Marco Casazza and Pedro L. Lomas

Received: 15 April 2022

Accepted: 6 June 2022

Published: 8 June 2022

**Publisher's Note:** MDPI stays neutral with regard to jurisdictional claims in published maps and institutional affiliations.



**Copyright:** © 2022 by the authors. Licensee MDPI, Basel, Switzerland. This article is an open access article distributed under the terms and conditions of the Creative Commons Attribution (CC BY) license (<https://creativecommons.org/licenses/by/4.0/>).

## 1. Introduction

In recent years, the offshore wind energy industries have rapidly developed all over the world, because wind energy is clean and sustainable. The new offshore wind installed capacity worldwide is 6068 MW in 2020, and China contributed half of it [1] (p. 47). Benefiting from the fewer geographical limits, offshore wind farms generally have more wind turbines than onshore wind farms and the arrangement of turbines is able to be tighter. Thus, offshore wind farms have more significant impacts on the planet boundary layer (PBL). At the same time, before a new wind farm is established, the design of wind turbine arrangements with the least influence by wake, and the study of micrometeorological variations brought by wind farms, are essential for achieving the best economic and environmental benefits. Based on the above, this research concerns the accuracy of offshore wind farm wind wake simulation for the physical process in operation.

In another aspect, a grand challenge for the development of wind energy is the connection between wind farms and electric grids [2]. The power production is intermittent

and random due to the time-variation wind speed, and thus an accurate power forecast is important for the promotion of wind energy. Generally, there are two kinds of methods of wind power forecasting, statistical methods and physical methods [3,4]. Based on the historical data of wind farms, the statistical methods predict the wind speed or output power mainly by the means of machine-learning methods (such as the artificial neural network [5] and support vector machine [6]) coupled with intelligent algorithms (such as particle swarm optimization [7], genetic programming [8], and the dragonfly algorithm [9] et al.). Recent studies in this field highlight the methods based on support vector regression (SVR) [10]. The hybrid models composed of SVR and wavelet transform perform well in predicting the wind speed [11] and the ramp event [12]. Moreover, when the bilateral Gaussian wake model is inputted into the SVR model, the method is capable of exploring the optimal placement of turbines in addition to wind speed prediction [13].

Compared with the statistical methods, the physical methods have their own characteristics. Although the accuracy of power forecasting is not better than the statistical methods, the physical methods have the ability to represent wind power plant aerodynamics with finer wake models, which can be further studied for the simulation of the wake turbine interference and its loads on downwind turbines. Then, the physical methods turn the wake visualization into reality. Moreover, to gather the information of renewable energy for long-term planning, the implementation of registries is discussed and studied [14]. A method that estimates power generation by numerical simulations with open access weather data is essential when the feed-in time series of wind plants are not publicly available [15]. Due to the above, the studies of physical methods for the simulation of wind farms are necessary, especially for the wind farms with limited data.

## 2. Literature Review

The physical models representing the interaction between wind farms and the atmosphere are generally distinguished with different scales [16]. The coarsest approach treats the wind farm as additional surface roughness or a drag force [17–19]. Due to the computational cost not being expensive, the completely static methods are adequate for simulating the impact of wind farms on the atmospheric boundary layer on a global or a relatively large scale. However, due to lack of the simulation of the turbulence caused by turbines, these approaches are not enabled to reflect the operating status of wind farms. In addition, relatively few observations lead to the difficulty of choosing the right roughness value in the practice.

In contrast, other methods attempt to resolve the turbulence on a fairly small scale. As the mesh becomes finer, the computational fluid dynamics (CFD) methods coupled with the mesoscale numerical weather prediction are employed to reflect the flow field in the wind farm or the wake structure generated from wind turbines [16]. For instance, large eddy simulation (LES), one of the CFD methods, allows resolving the turbulence with a high resolution of about 10 m [20–23]. Meanwhile, the small grid space makes the calculation more complex, resulting in these approaches being too much computation to be applied in the real operation.

Between the wind turbine scale and the synoptic scale models, the wind farm scale models have the advantage of balancing the accuracy and computational time of simulation [16]. Various models have been developed in recent years, and they generally parameterize the wind turbine as a sink of momentum and a source of turbulence [24–26]. With different methods of representing the turbulence/wake induced by the wind turbine, these models simulate the interactions between the wind farm and the atmospheric boundary layer by taking the thrust curve and power curve to represent wind turbines. However, the relatively larger scale indicates that turbulence in a grid cell is not resolved, and as a result, the effect of one turbine on another is not presented if they are inserted into the same grid.

Compared to other mesoscale wind farm models, the wind farm parameterization (WFP) scheme developed by Fitch et al. has been widely employed in past studies for its

open availability and ease of operation. This scheme owns the capability of simulating the wake and the power capacity of wind turbines in wind farms, and the wind farm's influence on local meteorological variables [24], such as heat flux, temperature, and humidity. Some of the previous studies have evaluated the performance of the WFP scheme in simulating the wake by comparisons with LES models [27,28], the measurements [29,30], and the other mesoscale physical scheme [31–33]. Other avenues of research include the impacts of the wind farm on local climate [34] or power generation [32,35,36]. Though the WFP scheme still has some limits [37], and there are approaches for further improvement [38], its capability can be accepted because of its simulations showing good agreement with observations.

The past studies conducted many sensitivity experiments in terms of operating conditions, including the horizontal and vertical resolutions [39–44], the Turbulence Kinetic Energy (TKE) option [41,43], and other configurations of the Weather Research Forecast (WRF) model (such as the time step and the WRF version) [41]. Their results suggest that the horizontal and vertical resolution are more influential than other factors in the simulation of wind speed, and the TKE option is essential. This research provides references of configurations for this study.

The applications of the WFP scheme on real wind farms are noticeable. For example, the ability of the power forecast is useful, and it has also been validated by the previous works with measurements [39,40]. As an important aspect of the WFP, the simulation of the micrometeorological impacts brought by wind farms has been evaluated with aircraft observations [44]. In the work of Vanderwende and Lundquist [45], the WFP scheme is coupled with the WRF model, and the crops are presented at different roughness lengths to test the influence of agriculture on power production. Moreover, Wang et al. [46] simulated the wind speed loss caused by a GW large onshore wind farm and its impacts on the atmospheric boundary layer, and the result can be used to test the risk of sand dust weather brought by wind farms for a nearby city. In addition, Wang et al. [47] examined the interaction between two onshore wind farms, which is a meaningful work for the owner of wind farms.

The previous works are relatively comprehensive, but there are still deficiencies. The research on the effect of the horizontal downsize method at different locations has not yet been studied, and the sea–land atmospheric effects need to be understood with a more comprehensive analysis. As a result, this paper has the following contributions:

1. The accuracy of simulating the wind speed and power production is validated, including the performance of the downsizing method in the different locations inside the wind farm.
2. The transition from the sea to the land has some impacts on the simulation of the flow field in the area near the coastline, and these influences are discussed. Moreover, except for the velocity, the variations of vorticity are taken into consideration.

Therefore, this article has two topics. For the first topic, the downsizing method is employed by setting different horizontal resolutions, and the results are compared with measurements and analyzed quantitatively and qualitatively. Turbines located in different locations are selected to test the spatial performance of the horizontal downsize method. The other topic focuses on the special atmospheric phenomenon near the coast and around the offshore wind farm. The spatial distributions of velocity and vorticity magnitude under different situations are presented and discussed, as the sea–land atmospheric effects and the impacts of the offshore wind farm on the flow field are reflected by the changes in wind speed and vorticity.

The structure of this paper is laid out as follows. Section 1 introduces the background of the research and Section 2 is a literature review. Section 3 describes the mathematical descriptions of the WFP scheme, measurements, and the simulation configurations. The introduction of the offshore wind farm is in Section 4. In the first part of Section 5, the accuracies of the simulations in wind speed and power production are validated, as well as the effect of the downsize method at different sites inside the wind farm. In the second

part of Section 5, the sea–land atmospheric effects and the variations of the flow vorticity brought by the offshore wind farm are shown and described. The results of the experiments are discussed in Section 6. In the last section, the authors conclude this paper to illustrate the impact of this work and future studies in the next steps.

### 3. Research Methods

#### 3.1. Description of the Mathematical Model

In the investigation, we used the WFP scheme coupled with WRF V4.0 [48] to simulate the operation of wind turbines. There is a brief introduction to WFP here, and more details are in Fitch et al. [24]. In the WFP scheme, wind turbines extract kinetic energy from the atmosphere as drag force work:

$$F_{drag} \cdot |V| = \frac{1}{2} \rho |V|^2 C_T A |V|, \quad (1)$$

where  $V$  is the horizontal wind speed. The thrust coefficient of the wind turbine is  $C_T$ , varying with the variation in  $V$  in the WFP scheme.  $\rho$  is the air density.  $A$  is the rotor plane area, and its value is  $(\pi D)^2/4$ , where  $D$  is the diameter of the turbine rotor plane. Moreover, turbines are always facing the inflow by default in the WFP scheme, and hence the yaw angle is zero.

In this model, as the mechanical and electrical losses are negligible, the drag force work is divided into two parts: one is the electric energy while the other is the Turbulence Kinetic Energy (TKE), as presented in Figure 1. The rate of electric energy produced by wind turbines can be given by the following equation:

$$P = \frac{1}{2} \rho |V|^2 C_P A |V|, \quad (2)$$

where  $C_P$  is the power coefficient, varying with the variation in  $V$  in the WFP scheme.

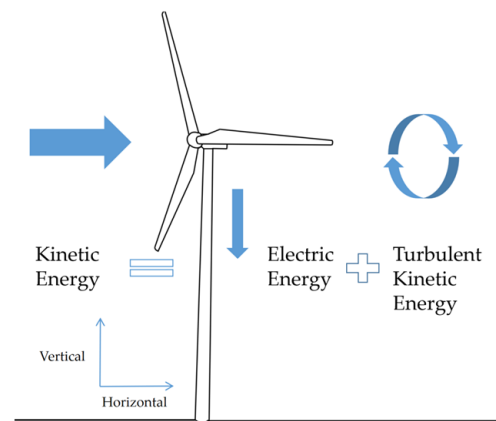


**Figure 1.** A brief diagram of the WFP scheme.

The TKE represents the influence of wind turbines on atmospheric airflow. The upper-level flow mixes with the lower-level flow with rotation of the wind turbine blades, making changes to the wind speed vertical component. The WFP accounts for the TKE in a grid cell by the following:

$$\frac{\partial TKE_{ijk}}{\partial t} = \frac{\frac{1}{2} N_t^{ij} C_{TKE} |V|_{ijk}^2 A |V|_{ijk}}{z_{k+1} - z_k}, \quad (3)$$

where  $i$  and  $j$  are the zonal and meridional coordinates of the model grid cell, and  $k$  is the vertical level of the model. The horizontal density of wind turbines in the grid cell  $(i, j)$  is defined as  $N_t^{ij}$ , and  $z_k$  is the height of the model level  $k$ . The parameter  $C_{TKE}$  is a dimensionless number, and  $C_{TKE}$  equals the thrust coefficient minus the power coefficient in

the numerical simulations, though these two coefficients are different in physical meaning. The above equation defines the rate of change in TKE per unit mass of air in a specific grid cell.

### 3.2. Measurements

This research relies on the data recorded by the wind turbines' Supervisory Control and Data Acquisition (SCADA) system. The SCADA system outputs every 10 min of wind turbine operating data, including wind speed and power production. Figure 2a shows the equipment for wind speed observation in the SCADA system and Figure 2b presents the location of anemometers. The equipment for the measurement of wind speed consists of two wind vanes and two 3-cup anemometers, and they are located at the rear of the nacelle. Although the anemometers are behind the rotor, the output wind speed can be viewed as the value in front of the rotor, as the measured values are corrected by algorithms.

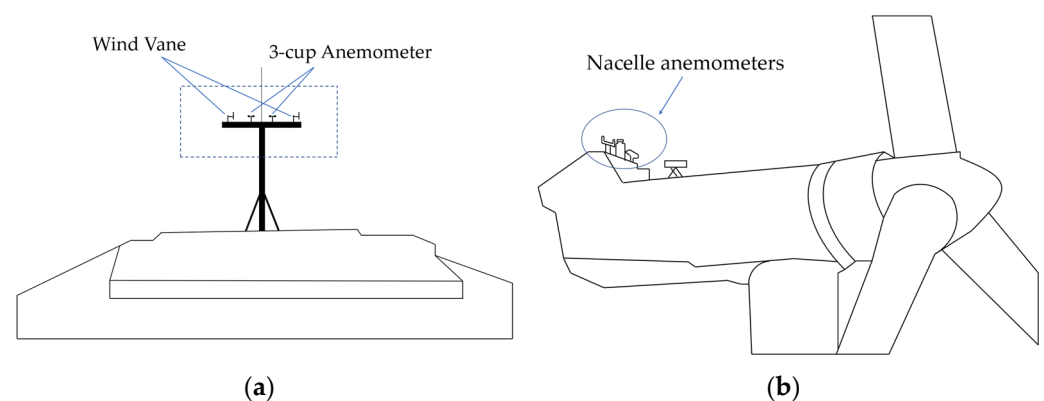


**Figure 2.** The structure and location of the observation instruments for wind speed in the SCADA system: (a) two wind vanes and two 3-cup anemometers are used to measure the wind speed; (b) the anemometers are at the rear of the nacelle.

### 3.3. Simulation Methods

The study simulates a 48 h period from UTC 18:00 on 22 January 2020 to UTC 24:00 on 25 January 2020 with a spin-up time of 6 h, in which the wind speed was at a range of 6 m/s to 11 m/s with a nearly constant northeast wind direction. The boundary and initial conditions were provided by the NECP's 0.25° Global Forecast System (GFS) reanalysis datasets. There are three cases in the research, and the differences between the cases are the horizontal resolutions. The different horizontal resolutions are employed to study the effect of the downsizing method.

Case III with three domains is the baseline case in the research, and the whole wind farm is inserted into the model, as Figure 3 presents. Furthermore, the research of sea-land effects is based on Case III. The relationships between different cases and the steps of the experiments are shown in Figure 4. In Case III, the simulation is running with three domains whose horizontal resolutions are 12 km (d01), 3 km (d02), and 1 km (d03), and the number of grid points in the horizontal plane are  $200 \times 200$  (d01),  $201 \times 201$  (d02), and  $202 \times 202$  (d03), respectively. In order to test the accuracy of simulations under different horizontal resolutions, Case I has only one domain, whose horizontal resolution and the number of grid points are the same as the first domain of Case III, while Case II has two domains that agree with the first two domains of Case III in the horizontal resolutions and numbers of grid points. The whole wind farm is added into the finest domain of the above three cases. In all the cases, the central area of the domains in the simulations, where the wind farm is, is covered by the finest domain completely. Additionally, the vertical resolution is 10 m below 200 m above sea level, and this meshing method is used in all cases.

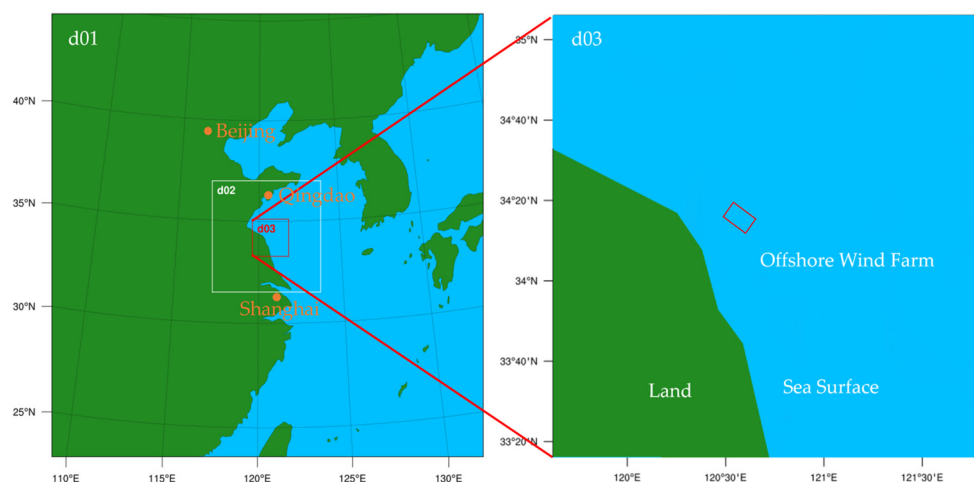


Figure 3. The domains of Case III and the relative location between the offshore wind farm and coastline.

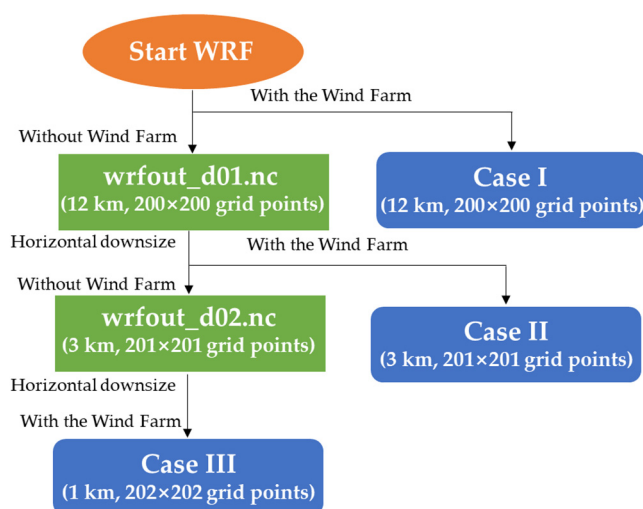


Figure 4. The flow chart of the experiments in the research.

The procedure of this study is described in the following. At first, WRF is operating with only one domain (d01), and the wind farm is added into the d01. This is the operating course of Case I. Then, WRF is operating with d01 and the wind farm is not in the model, and the result file is marked as wrfout\_d01.nc. This is followed by downsizing the horizontal grid space based on wrfout\_d01.nc and obtaining the boundary and initial conditions for the WRF operation with d02. If the wind farm is inserted into the model, the result is Case II, otherwise, the result is wrfout\_d02.nc. At last is downsizing the horizontal grid space based on wrfout\_d02.nc and running WRF with the wind farm, and the result is Case III.

The configurations of the number of grids and the finest horizontal resolution employed in this study are considered. The first reason is that the research object is an offshore wind farm in this article, meaning that the impacts of terrain on the wind speed simulation can be ignored and the coarser horizontal resolution is acceptable. The second reason is to ensure the timeliness of the methodology when it is used in reality. The whole forecast time interval is 54 h, and the first 6 h is the spin-up time. According to the timescale classification [49], this research can be viewed as a medium-term forecast. With the equipment employed in the research, the operation time of Case III is about 36 h, which means that the method has the timeliness for the usage of power forecast.

As for the physics options, the PBL scheme for operating WRF is the MYNN 2.5 [50]. A Thompson aerosol-aware scheme [51] was chosen for the microphysics process. The longwave parameterization is the RRTMG scheme [52], and the shortwave parameterization

is the Dudhia scheme [53]. The surface layer model employed is the revised MM5 surface layer scheme [54], with a choice of Noah land surface scheme [55]. At last, the cumulus parameterization is the Grell–Devenyi ensemble scheme [56].

The equipment employed in the research is Centos 7 with 64 Intel Gold Xeon cores, and the capacity of memory is 256 G.

#### 4. Study Area

An offshore wind farm operated by the CDT group with 100 wind turbines, located about 10 km from the coast of Jiangsu province, China, is the data resource. The wind farm is divided into two regions presented in Figure 5, in which region A contains 3 rows and 56 wind turbines, and region B contains 2 rows and 44 wind turbines. A blank zone with a 3 km width separates the two regions. The type of wind turbine from NO.1 to NO.50 is Turbine 1, while the last turbines are Turbine 2, and their parameters under the ideal condition provided by manufacturers are listed in Table 1.

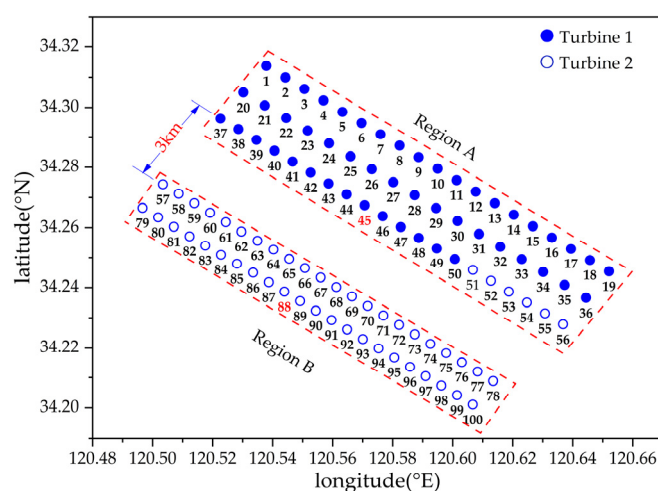


**Figure 5.** The wind turbine arrangement in the offshore wind farm and the division of region A and region B. Two different types of wind turbines are presented in solid and hollow dots, respectively. Red numbers mark the wind turbines selected to be analyzed in this research.

**Table 1.** The parameters of two types of wind turbines used in the wind farm.

Wind Turbine Parameters	Turbine 1	Turbine 2
Rated Power (KW)	3000	3300
Rotor Diameter (m)	135	140
Hub Height (m)	90	91
Cut in Wind Speed (m/s)	3	2.5
Cut out Wind Speed (m/s)	25	20
Rated Wind Speed (m/s)	10	11

## 5. Results

### 5.1. Performance of Wind Speed and Power Simulations

#### 5.1.1. Wind Speed Simulation on the Hub Height

The accuracy of wind speed is the basement for a more accurate power forecast. The wind speed and direction discussed in this study are the values on the hub height of wind turbines, as the measuring instruments record the data on the hub height. The first 6 h of 54 h is the spin-up time, and it is not taken into account in the analysis. In the selected period, the wind direction is almost constant northeast, as presented in Figure 6, especially after 36 h, which is convenient for the analysis owing to that wind turbines behind the first row are downwind. To reflect the general trend of wind speed and direction clearly, data per 1 h are plotted in figures, but data per 10 min are analyzed in this study. Additionally, the

simulation data are instantaneous values, while the measurement data are averaged values. They are compared straightly in the research due to the coarse simulation of turbulence in the mesoscale model, making the perturbation ignored. Furthermore, only the simulation data from the finest domain of each case are employed due to the WFP scheme being inserted into the finest domain.

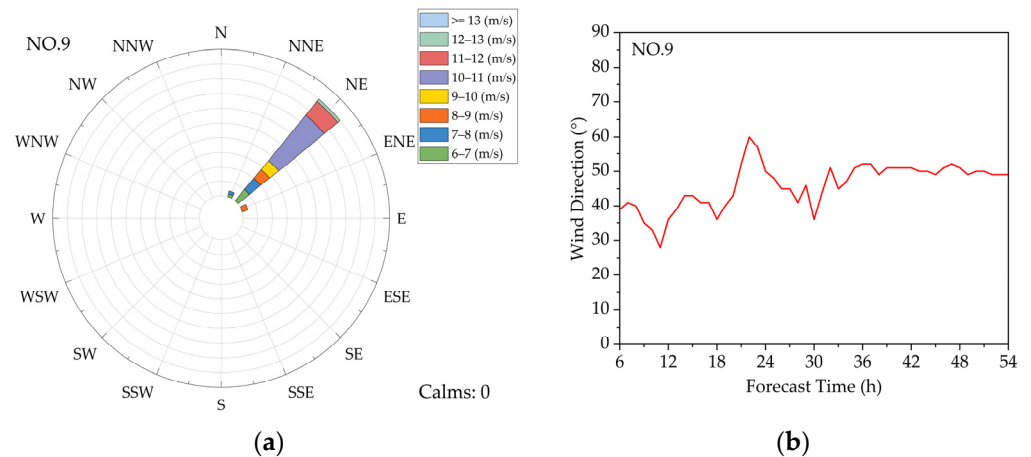


**Figure 6.** A description of the wind direction during the simulation period: (a) the wind rose of NO.9 turbine on the hub height; (b) wind direction varies with time.

In the model, the wind speed deficits downwind are decided by the local and upwind turbines, thus the accuracy of the wind speed for the turbines in different rows needs to be discussed. Two turbines on the wind farm, one of which is in the last row of Region A (NO.45 turbine) and the other in the last row of Region B (NO.88 turbine), were chosen as the research objects. Moreover, the effect of the downsizing method is worth investigating. First, the wind speed of Case I, Case II, Case III, and observation data from NO.45 and NO.88 turbine are drawn in Figure 7 to facilitate a discussion regarding the impact of the horizontal resolutions and turbine location on the simulation of wind speed.

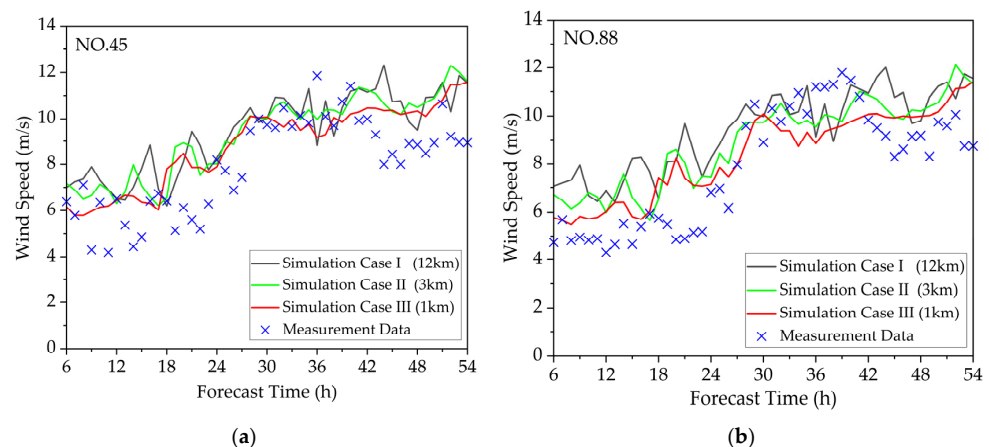


**Figure 7.** The simulation results and measurement data of wind speed for NO.45 and NO.88 turbine: (a) the temporal distribution of wind speed from observation data and simulation results with three horizontal resolutions for NO.45 turbine; (b) the temporal distribution of wind speed from observation data and simulation results with three horizontal resolutions for NO.88 turbine.

Figure 7 shows that the wind speed and its variation are similar between simulated and observed values for both two turbines, making a consequence that simulated wind speed can be qualitatively applied for power simulation. In addition, wind speeds in the simulations are higher than the measurement values most of the time. The downsize method shows its advantage, as the lines in Figure 7 have a clear stratification. With the

decreasing of the horizontal resolution, the simulation results move down, and as a result, the line is closer to the observation data for much of the time. The exception is from 30 h to 39 h, as the observed wind speed is at a high level.

To validate the simulation of wind speed on the whole wind farm, the quantitative analysis is essential, and the comparisons between simulations and measurement data from two wind turbines in the different rows need to be illustrated. Furthermore, the performance of the downsizing method should be assessed by the quantitative indexes. The choice of parameter for the quantified analysis in this study is the Root Mean Squared Error (RMSE) for its higher weight [57]. The RMSE are calculated in Table 2, and it is defined as:

$$RMSE = \sqrt{\frac{1}{n} \sum_{i=1}^n (\hat{x}_i - x_i)^2}. \quad (4)$$

**Table 2.** The RMSE of wind speeds for selected turbines with different horizontal resolutions.

Horizontal Resolution (km)	NO.45 Turbine	NO.88 Turbine
12	1.93 <sup>1</sup>	2.03
3	1.82	1.65
1	1.52	1.44

<sup>1</sup> The unit in this table is m/s.

In the above equation,  $\hat{x}_i$  represents data of a single simulation while  $x_i$  is the corresponding measurement data.

Quantitatively, both the RMSEs have ideal performance compared with other studies [39,46]. The downsize method makes significant progress in the simulation of wind speed. Regarding the NO.45 turbine, for example, when the size of grids turns from 12 to 1 km, the RMSE decreases about 21.2%, to 0.41 m/s. It indicates that a finer horizontal resolution captures the wind deficits in more detail inside the wind farm. Moreover, the degree of increase in the accuracy of simulations varies with the different turbines. In the aspect of RMSE, it decreases from 1.93 to 1.52 m/s on the NO.45 turbine, and as a comparison, it decreases from 2.03 to 1.44 m/s, about 29%, on the NO.88 turbine. Furthermore, when the horizontal resolution is 12 km, the simulation of the NO.45 turbine is more accurate than that of NO.88 turbine, while the reverse applies under two other horizontal resolutions.

The results suggest that the simulation data of the upwind turbine are closer to the measurement data. One of the reasons is that the power out is restricted some of the time, as described below. The power production does not agree with the power curve, making the real wind speed higher than predicted. Although the results are influenced by the operation of the wind farm, the model with a horizontal resolution of 1 km performs well in the simulation of wind speed.

### 5.1.2. Turbine Power Forecast

The assessment of power simulation is also important for the evaluation of WFP's performance. AS with the validation of the wind speed, the investigation selected two wind turbines from different rows to test the error of simulation, and the observation data of power production for the selected wind turbines are shown in Figure 8 with the simulation results of Case III.

In Figure 8, the model results agree well with the measurement data from 6 to 18 h. Unfortunately, there is a huge bias when the forecast time is in the range of 19 to 24 h, corresponding to the error in wind speed simulation presented in Figure 7 at the same time. Furthermore, in Figure 8b, it is significant that the power productions of wind turbines are restricted to protect the wind turbines from overheating in the time interval from 26 to 40 h and from 45 to 54 h, in which the areas are colored by yellow. The power restricted points are shown straightly in Figure 9, as some of the observation points deviate far from the manufacturer's power curve, while the wind shear in vertical resolutions is rarely so

influential [58]. Although another turbine is not as obvious as the NO.88 turbine in limiting the power output, the data points covered by the yellow rectangle are excluded to make the standard uniform when calculating the RMSEs listed in Table 3.

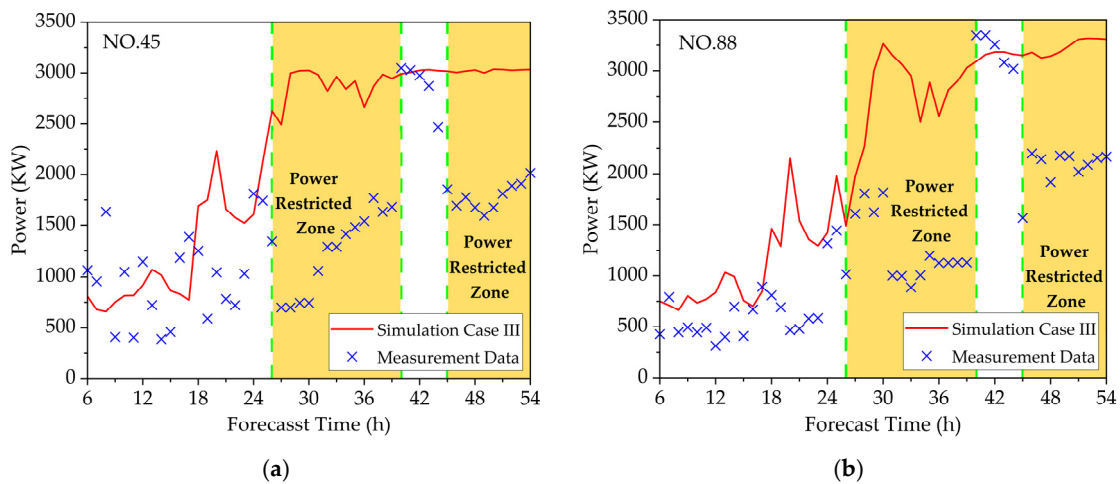


**Figure 8.** The simulation results from Case III and measurement data of power production for the selected wind turbines: (a) NO.45 turbine; (b) NO.88 turbine.

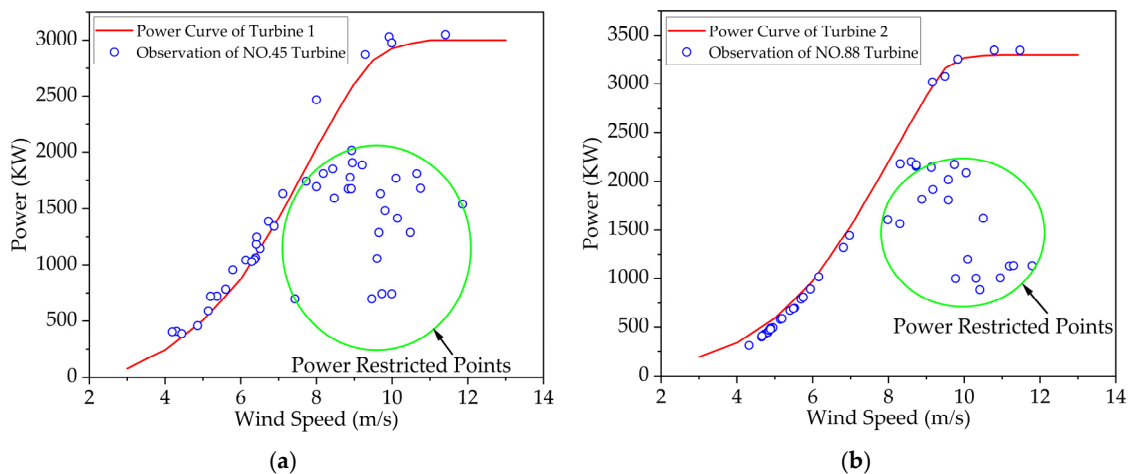


**Figure 9.** The power curve and power observation values for the chosen wind turbines: (a) power curve for Turbine 1 and power observation values for NO.45 turbine; (b) power curve for Turbine 2 and power observation values for NO.88 turbine.

**Table 3.** The RMSE of power productions for selected turbines.

Number of Turbines	RMSE (KW)
45	561.53
88	550.16

The variation trend of power error in Table 3 resembles that of wind speed error in Table 2. The power simulation of the NO.88 turbine is a little more accurate than that of the NO.45 turbine. The decreases are also worthy of attention, with 2% of RMSE, and all the errors are not larger than the 20% of the rated power. This demonstrates that the accuracy of the power simulation relies on the simulation of the wind speed, and the influence of overestimating the wind deficits is more significant on the power simulation.

### 5.2. Sea–Land Atmospheric Effects and Vorticity in the Model

To represent the spatial distribution of the flow field straightly, two time points were selected to be analyzed in this section, 16 h and 40 h. In this section, the wind speeds are the values at 90 m above sea level, the hub height of turbines in the wind farm. At 16 h, the inflow wind speed of the wind farm is about 7 m/s, while the inflow wind speed is about 10 m/s at 40 h. The spatial distribution of wind speed for the two time points under Case III in the wind farm area is represented in Figure 10.

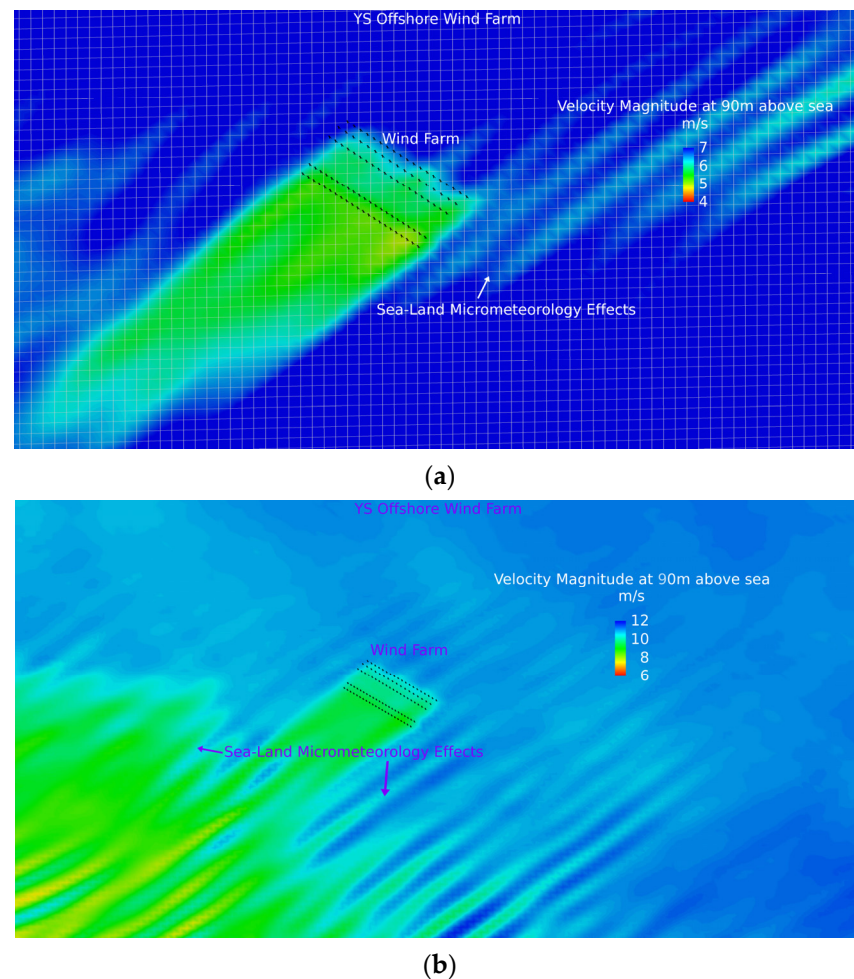


**Figure 10.** The diagram of wind speed around the wind farm at 16 h and 40 h: (a) the spatial distribution of wind speed on the hub height at 16 h under Case III; (b) the spatial distribution of wind speed on the hub height at 40 h under Case III.

It is demonstrated that the large-scale offshore wind farm has changed the flow field of the sea surface already, and the transition from the sea to land has impacted the simulation of wind speed from the model results. In Figure 10, the existence of the offshore wind farm causes the deficits of wind speed. On the boundary of land and sea in Figure 10b, the distribution of wind speed is irregular, due to the anomalous reduction on the sea surface near the land. Moreover, the scope of sea–land atmospheric effects is larger, and the wind farm is covered in Figure 10a. Compared with the higher inflow wind speed, the sea–land atmospheric effects are more influential with a lower inflow velocity.

Another project analyzed is the spatial distribution of vorticity. In the WRF + WFP model, the impacts of the wind farm are illustrated not only by the wind speed but also by the vorticity magnitude. The vorticity magnitude at 30 m above sea surface with a 10 m/s inflow is presented in Figure 11, and the sea–land atmospheric effects are more significant with a clear dividing line between the sea and land.

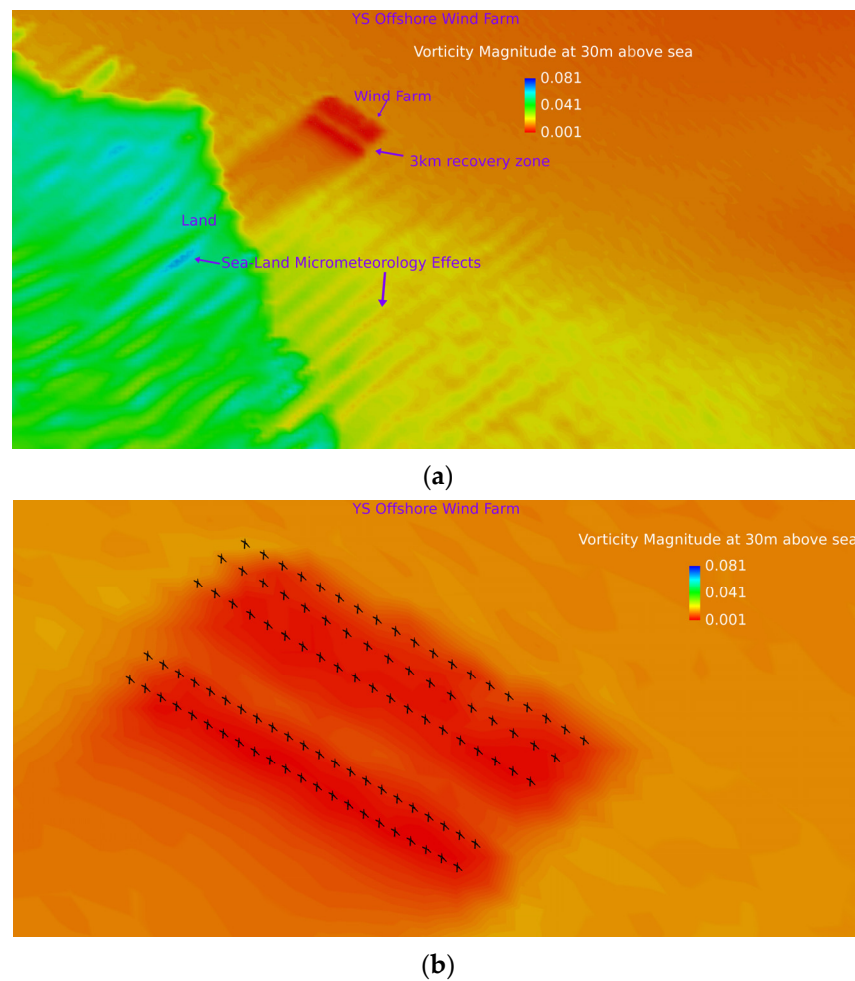


**Figure 11.** The diagram of vorticity magnitude at 30 m above the sea with an about 10 m/s inflow velocity under Case III: (a) the vorticity magnitude on the land and sea; (b) the vorticity magnitude around the wind farm.

Contrary to the wind velocity, the vorticity magnitude is increasing in the land area in Figure 11a. This suggests that the land reduces the flow velocity and increases the vorticity at the same time. However, the performance of the wind farm is different from that of land. The model result shows that both the wind speed and vorticity magnitude are decreasing in the wind farm and wake area, and the vorticity is smallest in the grids containing wind turbines, where the values of vorticity are close to 0. Thus, the 3 km recovery zone between the two regions makes an appearance in the recovery of the vorticity of the ambient flow in Figure 11.

The sea–land atmospheric effects are reflected by the spatial distribution of the vorticity represented in Figure 11a as well. In the coastal region, the vorticity has irregular additions both on the land and sea surface. It means that the transition between the land and sea is capable of increasing the vorticity, and compared with the sea–land atmospheric effects on the velocity magnitude, the variations of vorticity have fewer influences on the offshore wind farm.

## 6. Discussion

### 6.1. Discussion of Wind Speed and Power Simulations

The modeling and simulation scheme (WRF + WFP) is shown to be a useful tool to compute and simulate the wind speed and power forecast of wind turbines in an offshore wind farm, capturing the farm aerodynamic reality at an affordable computation expense (36 h of computation time on a 64 core 256 GB Ram workstation). The accuracies of

simulations of wind speed and power production from two single turbines on the farm were evaluated against the measurement data to study the effects of the mesh downsize refinement method (nesting grid using NDOWN in WRF). The horizontal downsize method increases the accuracy of wind speed simulation, and the effect is more significant at the downwind turbine (NO.88) than at the upwind turbine (NO.45). When the size of the grids is  $12 \text{ km} \times 12 \text{ km}$ , the upwind turbines and the downwind turbines are inserted into the same grid, and the simulated values of wind speed at all turbines are the same as that at the turbines in the first row. As the wind speed deficits become more and more serious from the first row to the last row, the simulated value of wind speed is closer to the wind speed at the upwind turbines than that at downwind turbines. Thus, the increasing range of the wind speed simulation accuracy is larger at downwind turbines than that at upwind turbines when the horizontal resolution increases from 12 to 1 km.

The MAE and RMSE of the power production forecast computations have similar variation trends with that of wind speed, although the power-limited zones (due to grid integration issues) are excluded when the indexes are calculated. Furthermore, the broken lines of the power forecast in Figure 8 have the same time-variation trend as the broken lines of the wind speed simulation in Figure 7 before the wind speed reaches the rated wind speed. This indicates that the accuracy of the power forecast is on the basement of the accuracy of the wind speed simulation. In the WRF + WFP model, the power output is calculated by the inflow wind speed and the power curve. According to Equation (2), the relationship between the wind speed and the power is cubic in the range from the cut-in wind speed to the rated wind speed, and as a result, the error of the power forecast can be huge when there is a small error in the simulation of wind speed.

### 6.2. Discussion of Sea–Land Atmospheric Effects and Vorticity

The sea–land atmospheric effects are due to the influences of land on the sea surface flow field in the model. When the wind is from the sea to the land, there is a reduction in the wind speed caused by the land, and the vorticity of wind becomes larger with the variation in the surface. These effects brought by the land expand to somewhere on the sea surface and have impacts on the simulation of the wind farm, especially when the inflow wind speed is small. For example, in Figure 10a, the wind speed deficits caused by the sea–land atmospheric effects are near to that caused by the wind farm. The superposition of the above two resources causes the uneven distribution of wind speed within the wind farm, resulting in underestimating the inflow velocity of wind turbines and decreasing the power forecast accuracy.

The investigation of vorticity supplies a new approach to understanding the performance of the WRF + WFP model. In this model, the offshore wind farm causes a decrease in vorticity magnitude, which is different from the simple roughness models equal to the land in this study. Compared with other regions (such as the 3 km recovery zone within the offshore wind farm), the vorticity reducing effect is most obvious in the turbine-containing grids, and these grids are the momentum sink resources on the mean flow as well. When the kinetic energy of the flow is transformed into electrical power and turbulent kinetic energy, the vorticity of the flow field becomes smaller and close to zero. This is a special discovery of this study.

## 7. Summary

For the first time, the WRF + WFP modeling and simulation scheme was deployed to study an existing offshore wind farm in the China Yellow Sea for wind speed and power forecasts for a 48 h simulation that correlated with two wind turbines' SCADA data. At the same time, the wind power plant aerodynamics with turbine farm wake effects and some interesting sea–land micrometeorology effects were shown and investigated using vorticity magnitude analysis. This modeling method is physical-based and is found to be suitable for scientific research on wind power plant aerodynamics and its nearby environmental micrometeorology evaluations. Authors believe that with future development, the

method may be a powerful tool to guide the active operation and maintenance of offshore wind farms.

In this research study, it was found that the horizontal downsize method is effective to capture farm turbines' wake downwind, which can prolong more than 10 km in the velocity field, especially for higher incoming wind velocity, and the accuracy of the power forecast was found to be improved for higher wind speed simulations. Moreover, the power-restricted operation in SCADA data and its impact on the power forecast was presented and was found to add some complexity to the correlation works.

Meanwhile, for the first time this study found some interesting wind speed disturbances, which may be caused by the sea–land atmospheric phenomena that should be further studied in future research. In this model, when the flow field switches from the sea to the land, a decrease in the wind speed and an increase in the vorticity magnitude was found. The results show that these effects have influenced the flow field in the area near the coast, particularly with a higher wind speed. As for the vorticity analysis of the flow field, the clear existence of the offshore wind farm was found, including 3 km separation region effects in the vorticity field analysis, and the interesting sea–land atmospheric effect as well.

It has to be pointed out that the wind direction data can be computed but were not studied due to lack of the measurement data from SCADA, but the research still illustrates that the WRF + WPF scheme is suitable for the simulations of the offshore wind farm. The application of the WRF + WPF scheme has brought new knowledge for the individual turbine level in a large wind farm power forecast and power plant aerodynamics with the hope to enable active operation and maintenance to achieve higher offshore wind farm performance.

As for the mesoscale forecasting models, an important application is the input of microscale models [59]. In future studies, the simulation results of mesoscale models can initialize the wind farm domain with a precursor volume field and be divided into planes according to time points (just like the time points presented in this article), with the planes used as the inflow boundary conditions of large eddy simulation, which is coupled with NREL's FAST turbine dynamics model. In this way, the turbine aerodynamics in a period of time can be simulated and the wake is able to be visualized. This is the reason why this work is also geared towards a better assessment of offshore wind power plant aerodynamics.

It was also found and learned through these studies that in future works different sizes of wind turbines should be used, or the model should be run and analyzed under different weather conditions. Furthermore, the power curves employed in this research are from the manufacturer's idealized power curves, while the real power curve is influenced by the temperature and pressure [58]. In this study, a particular time interval was selected, and the model was just operated once; therefore, more statistical data and strategies for simulation are required for the practical application under different conditions. It is necessary to simulate with adjusted turbine power curves to achieve a more accurate turbine power production prediction. In addition, the TKE advection was not employed in the research, which may impact the results. In any case, the WRF + WPF model is conducive to having a better understanding of the physical process of the interaction between the wind farm and atmospheric boundary layer, and the possibility of employing the model in the practical application of wind farms does exist.

**Author Contributions:** Conceptualization, Y.X. and Y.Z.; methodology, Y.X. and Y.Z.; software, Y.Z. and S.G.; validation, Y.Z., Q.C., T.S. and Y.L.; formal analysis, Y.Z.; investigation, Y.Z.; resources, Y.X.; data curation, Y.Z., Q.C., T.S. and Y.L.; writing—original draft preparation, Y.Z.; writing—review and editing, Y.X. and S.G.; visualization, Y.Z., Y.X. and J.W.; supervision, Y.X.; project administration, Y.X.; funding acquisition, Y.X. All authors have read and agreed to the published version of the manuscript.

**Funding:** This research was funded by the special fund for offshore wind power intelligent measurement and control research center and laboratory construction at Ocean University of China, grant number 861901013159.

**Institutional Review Board Statement:** Not applicable.

**Informed Consent Statement:** Not applicable.

**Data Availability Statement:** The software employed in the research is openly available in <https://github.com/wrf-model/WRF/releases> (accessed on 1 September 2020). The WFP scheme is in the package of the WRF model, and it is compiled together with the WRF model. The GFS reanalysis data can be downloaded from <https://rda.ucar.edu/datasets/ds084.1/> (accessed on 5 September 2020).

**Acknowledgments:** This research is supported by Ocean University of China and CDT Group.

**Conflicts of Interest:** The authors declare no conflict of interest.

### Abbreviations

The abbreviations employed in this article are listed in the following:

CFD	Computational Fluid Dynamics
GFS	Global Forecast System
LES	Large Eddy Simulation
MYNN	Mellor–Yamada–Nakanishi–Niino model
NECP	National Centers for Environmental Prediction
NREL	National Renewable Energy Laboratory
PBL	Planet Boundary Layer
RMSE	Root Mean Squared Error
SCADA	Supervisory Control and Data Acquisition System
SVR	Support Vector Regression
TKE	Turbulence Kinetic Energy
UTC	Universal Time Coordinated
WFP	Wind Farm Parameterization
WRF	Weather Research and Forecast Model

### References

1. Global Wind Energy Council (GWEC). Global Wind Report 2021. Available online: <https://gwec.net/wp-content/uploads/2021/03/GWEC-Global-Wind-Report-2021.pdf> (accessed on 27 October 2021).
2. Veers, P.; Dykes, K.; Lantz, E.; Barth, S.; Bottasso, C.L.; Carlson, O.; Clifton, A.; Green, J.; Green, P.; Holttinen, H.; et al. Grand challenges in the science of wind energy. *Science* **2019**, *366*, 6464. [\[CrossRef\]](#)
3. Jung, J.; Broadwater, R.P. Current status and future advances for wind speed and power forecasting. *Renew. Sustain. Energy Rev.* **2014**, *31*, 762–777. [\[CrossRef\]](#)
4. Hanifi, S.; Liu, X.; Lin, Z.; Lotfian, S. A Critical Review of Wind Power Forecasting Methods—Past, Present and Future. *Energies* **2020**, *13*, 3764. [\[CrossRef\]](#)
5. Marugán, A.P.; Márquez, F.P.G.; Perez, J.M.P.; Ruiz-Hernández, D. A survey of artificial neural network in wind energy systems. *Appl. Energ.* **2018**, *228*, 1822–1836. [\[CrossRef\]](#)
6. Zendejboudi, A.; Baseer, M.A.; Saidur, R. Application of support vector machine models for forecasting solar and wind energy resources: A review. *J. Clean. Prod.* **2018**, *199*, 272–285. [\[CrossRef\]](#)
7. Ren, C.; An, N.; Wang, J.; Li, L.; Hu, B.; Shang, D. Optimal parameters selection for BP neural network based on particle swarm optimization: A case study of wind speed forecasting. *Knowl.-Based. Syst.* **2014**, *56*, 226–239. [\[CrossRef\]](#)
8. Zameer, A.; Arshad, J.; Khan, A.; Raja, M.A.Z. Intelligent and robust prediction of short term wind power using genetic programming based ensemble of neural networks. *Energy Convers. Manag.* **2017**, *134*, 361–372. [\[CrossRef\]](#)
9. Li, L.; Zhao, X.; Tseng, M.; Tan, R.R. Short-term wind power forecasting based on support vector machine with improved dragonfly algorithm. *J. Clean. Prod.* **2020**, *242*, 118447. [\[CrossRef\]](#)
10. Dhiman, H.S.; Deb, D.; Balas, V.E. *Supervised Machine Learning in Wind Forecasting and Ramp Event Prediction*; Academic Press: Cambridge, MA, USA, 2020. [\[CrossRef\]](#)
11. Dhiman, H.S.; Anand, P.; Deb, D. Wavelet transform and variants of SVR with application in wind forecasting. In *Innovations in Infrastructure*; Springer: Singapore, 2019; pp. 501–511. [\[CrossRef\]](#)
12. Dhiman, H.S.; Deb, D. Machine intelligent and deep learning techniques for large training data in short-term wind speed and ramp event forecasting. *Int. Trans. Electr. Energ. Syst.* **2021**, *31*, e12818. [\[CrossRef\]](#)

13. Dhiman, H.S.; Deb, D.; Foley, A.M. Bilateral Gaussian Wake Model Formulation for Wind Farms: A Forecasting based approach. *Renew. Sustain. Energy Rev.* **2020**, *127*, 109873. [[CrossRef](#)]
14. Bieda, A.; Cienciała, A. Towards a Renewable Energy Source Cadastre—A Review of Examples from around the World. *Energies* **2021**, *14*, 8095. [[CrossRef](#)]
15. Lehneis, R.; Manske, D.; Thrän, D. Modeling of the German Wind Power Production with High Spatiotemporal Resolution. *ISPRS Int. J. Geo-Inf.* **2021**, *10*, 104. [[CrossRef](#)]
16. Porté-Agel, F.; Bastankhah, M.; Shamsoddin, S. Wind-Turbine and Wind-Farm Flows: A Review. *Bound.-Layer Meteorol.* **2020**, *174*, 1–59. [[CrossRef](#)]
17. Keith, D.W.; Decarolis, J.F.; Denkenberger, D.C.; Lenschow, D.H.; Malyshev, S.L.; Pacala, S.; Rasch, P.J. The influence of large-scale wind power on global climate. *Proc. Natl. Acad. Sci. USA* **2004**, *101*, 16115–16120. [[CrossRef](#)]
18. Kirk-Davidoff, D.B.; Keith, D.W. On the Climate Impact of Surface Roughness Anomalies. *J. Atmos. Sci.* **2008**, *65*, 2215–2234. [[CrossRef](#)]
19. Barrie, D.B.; Kirk-Davidoff, D.B. Weather response to a large wind turbine array. *Atmos. Chem. Phys.* **2010**, *10*, 769–775. [[CrossRef](#)]
20. Mirocha, J.D.; Kosovic, B.; Aitken, M.L.; Lundquist, J.K. Implementation of a generalized actuator disk wind turbine model into the weather research and forecasting model for large-eddy simulation applications. *J. Renew. Sustain. Ener.* **2014**, *6*, 013104. [[CrossRef](#)]
21. Nikola, M. Simulation of the Atmospheric Boundary Layer for Wind Energy Applications. Ph.D. Thesis, University of California, Berkeley, CA, USA, 2015.
22. Stevens, R.J.A.M.; Martínez-Tossas, L.A.; Meneveau, C. Comparison of wind farm large eddy simulations using actuator disk and actuator line models with wind tunnel experiments. *Renew. Energy* **2018**, *116*, 470–478. [[CrossRef](#)]
23. Arthur, R.S.; Mirocha, J.D.; Marjanovic, N.; Hirth, B.D.; Schroeder, J.L.; Wharton, S.; Chow, F.K. Multi-Scale Simulation of Wind Farm Performance during a Frontal Passage. *Atmosphere* **2020**, *11*, 245. [[CrossRef](#)]
24. Fitch, A.C.; Olson, J.B.; Lundquist, J.K.; Dudhia, J.; Gupta, A.K.; Michalakes, J.; Barstad, I. Local and Mesoscale Impacts of Wind Farms as Parameterized in a Mesoscale NWP Model. *Mon. Weather Rev.* **2012**, *140*, 3017–3038. [[CrossRef](#)]
25. Abkar, M.; Porté-Agel, F. A new wind-farm parameterization for large-scale atmospheric models. *J. Renew. Sustain. Energy* **2015**, *7*, 013121. [[CrossRef](#)]
26. Volker, P.J.H.; Badger, J.; Hahmann, A.N.; Ott, S. The Explicit Wake Parametrisation V1.0: A wind farm parametrisation in the mesoscale model WRF. *Geosci. Model Dev.* **2015**, *8*, 3715–3731. [[CrossRef](#)]
27. Eriksson, O.; Lindvall, J.; Breton, S.; Ivanell, S. Wake downstream of the Lillgrund wind farm—A Comparison between LES using the actuator disc method and a Wind farm Parametrization in WRF. *J. Phys. Conf. Ser.* **2015**, *625*, 12028. [[CrossRef](#)]
28. Vanderwende, B.J.; Kosović, B.; Lundquist, J.K.; Mirocha, J.D. Simulating effects of a wind-turbine array using LES and RANS. *J. Adv. Model. Earth Syst.* **2016**, *8*, 1376–1390. [[CrossRef](#)]
29. Siedersleben, S.K.; Platis, A.; Lundquist, J.K.; Lampert, A.; Bärfuss, K.; Cañadillas, B.; Djath, B.; Schulz-Stellenfleth, J.; Bange, J.; Neumann, T.; et al. Evaluation of a Wind Farm Parametrization for Mesoscale Atmospheric Flow Models with Aircraft Measurements. *Meteorol. Z.* **2018**, *27*, 401–415. [[CrossRef](#)]
30. Jiménez, P.A.; Navarro, J.; Palomares, A.M.; Dudhia, J. Mesoscale modeling of offshore wind turbine wakes at the wind farm resolving scale: A composite-based analysis with the Weather Research and Forecasting model over Horns Rev. *Wind Energy* **2015**, *18*, 559–566. [[CrossRef](#)]
31. Pryor, S.C.; Shepherd, T.J.; Barthelmie, R.J.; Hahmann, A.N.; Volker, P. Wind Farm Wakes Simulated Using WRF. *J. Phys. Conf. Ser.* **2019**, *1256*, 12025. [[CrossRef](#)]
32. Pryor, S.C.; Shepherd, T.J.; Volker, P.J.H.; Hahmann, A.N.; Barthelmie, R.J. “Wind Theft” from Onshore Wind Turbine Arrays: Sensitivity to Wind Farm Parameterization and Resolution. *J. Appl. Meteorol. Clim.* **2020**, *59*, 153–174. [[CrossRef](#)]
33. Shepherd, T.J.; Barthelmie, R.J.; Pryor, S.C. Sensitivity of Wind Turbine Array Downstream Effects to the Parameterization Used in WRF. *J. Appl. Meteorol. Clim.* **2020**, *59*, 333–361. [[CrossRef](#)]
34. Fitch, A.C.; Olson, J.B.; Lundquist, J.K. Parameterization of Wind Farms in Climate Models. *J. Clim.* **2013**, *26*, 6439–6458. [[CrossRef](#)]
35. Miller, L.M.; Brunzell, N.A.; Mechem, D.B.; Gans, F.; Monaghan, A.J.; Vautard, R.; Keith, D.W.; Kleidon, A. Two methods for estimating limits to large-scale wind power generation. *Proc. Natl. Acad. Sci. USA* **2015**, *112*, 11169–11174. [[CrossRef](#)]
36. Volker, P.J.H.; Hahmann, A.N.; Badger, J.; Jørgensen, H.E. Prospects for generating electricity by large onshore and offshore wind farms. *Environ. Res. Lett.* **2017**, *12*, 34022. [[CrossRef](#)]
37. Fitch, A.C. Notes on using the mesoscale wind farm parameterization of Fitch et al. (2012) in WRF. *Wind Energy* **2016**, *19*, 1757–1758. [[CrossRef](#)]
38. Archer, C.L.; Wu, S.; Ma, Y.; Jiménez, P.A. Two Corrections for Turbulent Kinetic Energy Generated by Wind Farms in the WRF Model. *Mon. Weather Rev.* **2020**, *148*, 4823–4835. [[CrossRef](#)]
39. Lee, J.C.Y.; Lundquist, J.K. Evaluation of the wind farm parameterization in the Weather Research and Forecasting model (version 3.8.1) with meteorological and turbine power data. *Geosci. Model Dev.* **2017**, *10*, 4229–4244. [[CrossRef](#)]
40. Lee, J.C.Y. Exploring the Role of the Atmosphere on Wind-energy Production: From Turbine Wakes to Variability of Wind Speed. Ph.D. Thesis, University of Colorado, Boulder, CO, USA, 2018.
41. Tomaszewski, J.M.; Lundquist, J.K. Simulated wind farm wake sensitivity to configuration choices in the Weather Research and Forecasting model version 3.8.1. *Geosci. Model Dev.* **2020**, *13*, 2645–2662. [[CrossRef](#)]

42. Mangara, R.J.; Guo, Z.; Li, S. Performance of the Wind Farm Parameterization Scheme Coupled with the Weather Research and Forecasting Model under Multiple Resolution Regimes for Simulating an Onshore Wind Farm. *Adv. Atmos. Sci.* **2019**, *36*, 119–132. [[CrossRef](#)]
43. Siedersleben, S.K.; Platis, A.; Lundquist, J.K.; Djath, B.; Lampert, A.; Bärfuss, K.; Cañadillas, B.; Schulz-Stellenfleth, J.; Bange, J.; Neumann, T.; et al. Turbulent kinetic energy over large offshore wind farms observed and simulated by the mesoscale model WRF (3.8.1). *Geosci. Model Dev.* **2020**, *13*, 249–268. [[CrossRef](#)]
44. Siedersleben, S.K.; Lundquist, J.K.; Platis, A.; Bange, J.; Bärfuss, K.; Lampert, A.; Cañadillas, B.; Neumann, T.; Emeis, S. Micrometeorological impacts of offshore wind farms as seen in observations and simulations. *Environ. Res. Lett.* **2018**, *13*, 124012. [[CrossRef](#)]
45. Vanderwende, B.; Lundquist, J.K. Could Crop Height Affect the Wind Resource at Agriculturally Productive Wind Farm Sites? *Bound.-Layer Meteorol.* **2016**, *158*, 409–428. [[CrossRef](#)]
46. Wang, Q.; Luo, K.; Wu, C.; Fan, J. Impact of substantial wind farms on the local and regional atmospheric boundary layer: Case study of Zhangbei wind power base in China. *Energy* **2019**, *183*, 1136–1149. [[CrossRef](#)]
47. Wang, Q.; Luo, K.; Yuan, R.; Zhang, S.; Fan, J. Wake and performance interference between adjacent wind farms: Case study of Xinjiang in China by means of mesoscale simulations. *Energy* **2019**, *166*, 1168–1180. [[CrossRef](#)]
48. National Center for Atmospheric Research (NCAR). A Description of the Advanced Research WRF Model Version 4. Available online: <http://n2t.net/ark:/85065/d7125x23> (accessed on 31 December 2021).
49. Rougvist, J.S.; Enevoldsen, P. Timescale classification in wind forecasting: A review of the state-of-the-art. *J. Forecast.* **2020**, *39*, 757–768. [[CrossRef](#)]
50. Nakanishi, M.; Niino, H. Development of an Improved Turbulence Closure Model for the Atmospheric Boundary Layer. *J. Meteorol. Soc. Jpn.* **2009**, *87*, 895–912. [[CrossRef](#)]
51. Thompson, G.; Eidhammer, T. A Study of Aerosol Impacts on Clouds and Precipitation Development in a Large Winter Cyclone. *J. Atmos. Sci.* **2014**, *71*, 3636–3658. [[CrossRef](#)]
52. Iacono, M.J.; Delamere, J.S.; Mlawer, E.J.; Shephard, M.W.; Clough, S.A.; Collins, W.D. Radiative forcing by long-lived greenhouse gases: Calculations with the AER radiative transfer models. *J. Geophys. Res.* **2008**, *113*, D1303. [[CrossRef](#)]
53. Dudhia, J. Numerical Study of Convection Observed during the Winter Monsoon Experiment Using a Mesoscale Two-Dimensional Model. *J. Atmos. Sci.* **1989**, *46*, 3077–3107. [[CrossRef](#)]
54. Jiménez, P.A.; Dudhia, J.; Gonzalez-Rouco, J.F.; Navarro, J.; Montavez, J.P.; Garcia-Bustamante, E. A Revised Scheme for the WRF Surface Layer Formulation. *Mon. Weather Rev.* **2012**, *140*, 898–918. [[CrossRef](#)]
55. Ek, M.B.; Mitchell, K.E.; Lin, Y.; Rogers, E.; Grunmann, P.; Koren, V.; Gayno, G.; Tarpley, J.D. Implementation of Noah land surface model advances in the National Centers for Environmental Prediction operational mesoscale Eta model. *J. Geophys. Res.-Atmos.* **2003**, *108*, 8851. [[CrossRef](#)]
56. Grell, G.A.; Devenyi, D. A generalized approach to parameterizing convection combining ensemble and data assimilation techniques. *Geophys. Res. Lett.* **2002**, *29*, 1693. [[CrossRef](#)]
57. Ogryzek, M.; Krypiak-Gregorczyk, A.; Wielgosz, P. Optimal Geostatistical Methods for Interpolation of the Ionosphere: A Case Study on the St Patrick’s Day Storm of 2015. *Sensors* **2020**, *20*, 2840. [[CrossRef](#)] [[PubMed](#)]
58. Saint-Drenan, Y.M.; Besseau, R.; Jansen, M.; Staffell, I.; Troccoli, A.; Dubus, L.; Schmidt, J.; Gruber, K.; Simoes, S.G.; Heier, S. A parametric model for wind turbine power curves incorporating environmental conditions. *Renew. Energy* **2020**, *157*, 754–768. [[CrossRef](#)]
59. Matthew Churchfield. Simulator for Wind Farm Applications (SOWFA). Available online: [https://www.aere.iastate.edu/nawea2017/files/2017/09/SOWFA\\_Training\\_NAWEA\\_2017.pdf](https://www.aere.iastate.edu/nawea2017/files/2017/09/SOWFA_Training_NAWEA_2017.pdf) (accessed on 24 March 2022).